Eur. Phys. J. B (2023) 96:76
https://doi.org/10.1140/epjb/s10051-023-00548-5

THE EUROPEAN PHYSICAL JOURNAL B

Regular Article - Computational Methods

Interaction of hydrogen with aluminum vacancies in the $Y_3Al_5O_{12}$ garnet and effects on positron trapping

A. G. Marinopoulos[a]

CFisUC, Department of Physics, University of Coimbra, Rua Larga, Coimbra 3004-516, Portugal

Received 21 March 2023 / Accepted 29 May 2023 / Published online 11 June 2023

Abstract. The introduction of hydrogen in the yttrium aluminum garnet, $Y_3Al_5O_{12}$ (YAG), has been known to affect the optical and luminescence properties of this material. This makes it imperative to examine the nature of hydrogen impurities in YAG and also to understand how hydrogen interacts with native defects. Recent studies based on positron-annihilation lifetime spectroscopy (PALS) provided strong evidence on the presence of hydrogen inside the YAG lattice that eventually led to strong reduction of the positron lifetimes attributed to cation-vacancy defects. The present study reports first-principles calculations that determine the character of isolated hydrogen states in the YAG solid as well as the interaction and binding of hydrogen to the aluminum monovacancies. A hybrid functional approach that incorporates exact electron-exchange interactions is employed to determine the defect association of aluminum vacancies with hydrogen and the charge-transition levels of the resulting vacancy-hydrogen complexes. The effects of hydrogen towards passivation were studied by means of two-component density-functional theory where the positron trapping and corresponding lifetimes of the vacancy defects were calculated as a function of the number hydrogen atoms bound to each vacancy. The final results are also discussed in connection with the experimental PALS data.

1 Introduction

The yttrium aluminum garnet, $Y_3Al_5O_{12}$, widely known as YAG, has a prominent place in technologies based on lasers, phosphors and scintillation devices, owing to its optical transparency and mechanical stability and hardness [1,2]. Point defects play an important role in the optical behavior of YAG. Extrinsic defects such as lanthanide dopants become luminescent activators providing the necessary optical transitions for energy conversion and photon emission [2–6]. It was also proposed that native point defects in the YAG lattice can act as deep or shallow traps for charge carriers and excitons, thus competing destructively with luminescence centers [3–5,7].

Effects of hydrogen in YAG single crystals were studied by optical absorption and thermo-luminescence measurements [8]. Hydrogen incorporation modified the optical absorption spectra and led to elimination of trap levels in the YAG band gap. The explanation given was that hydrogen binds to native defects and passivates their activity. It was also proposed by analysis of photo-luminescence measurements in undoped and Ce-doped YAG crystals that the presence of hydrogen during growth protects the Ce(3+) ions from oxidation and enhances luminescence intensity [9]. The strong interaction between hydrogen and native vacancy defects in YAG was clearly inferred in measurements and analysis by positron-annihilation lifetime spectroscopy (PALS) performed in YAG single crystals [10,11]. The PALS technique is well suited for the study of open-volume defects in solids, such as neutral or negatively charged monovacancies and vacancy clusters. Such defects can trap positrons since the potential sensed by the positron is lowered due to smaller repulsion by the positive-ion cores [12,13]. For the case of YAG, the negatively charged aluminum vacancies were proposed to be dominant trapping centers for positrons with the measured positron lifetimes ranging up to 280 ps, exceeding the bulk lifetimes of the YAG crystals by about 100 ps. Hydrogen introduced during crystal growth had a sizeable effect on the positron-annihilation characteristics. The most observable outcome was a strong reduction of the measured positron lifetimes. It was proposed that hydrogen atoms diffuse and bind at the aluminum vacancies, modifying the positron trapping at these sites [10]. These findings clearly suggest a strong association of hydrogen with the aluminum vacancies that needs to be addressed.

The native point defects of the YAG lattice have already been studied theoretically by means of both empirical [14,15] and first-principles calculations based on density-functional theory (DFT) [16–20], where it was shown that cation vacancies are high-energy

[a] e-mail: marinop@uc.pt (corresponding author)

defects. However, previous DFT calculations [16,19,21,22] for YAG were based on the local-density (LDA) and semilocal generalized-gradient approximations (GGA) for exchange and correlation [23]. The obtained band gap of YAG from these approaches ranged from 4.0 eV to 5.0 eV, thus appreciably underestimating the reported experimental gap with a magnitude of 6.5 eV [24].

In the present study DFT calculations were performed using the semilocal PBE functional together with the HSE06 hybrid-functional approach [25]. The latter incorporates a portion of exact exchange in the electron–electron interaction, an addition which is necessary to reproduce reliably the experimental band gap of YAG. Calculations of the formation energies and charge-transition levels were carried out to identify the lowest-energy states of the isolated hydrogen impurity in YAG as well as to quantify the defect association of hydrogen with the aluminum monovacancies.

The effects of hydrogen towards positron trapping in YAG were determined by calculations based on two-component DFT (TCDFT) [26–28], including gradient corrections to describe the electron–positron correlation. Previous TCDFT calculations of positron states of vacancy defects in YAG showed that inclusion of these corrections was necessary to explain the positron trapping at these defects and reproduce the bulk lifetimes obtained experimentally [19]. The positron states and the evolution of the positron lifetimes were determined for several vacancy-hydrogen defect complexes as a function of the number of hydrogen atoms bound to the aluminum monovacancies.

2 Theoretical background and preliminaries

The YAG lattice is body-centered cubic (space group $Ia3d$) with 80 atoms in the primitive cell [29,30]. The Al atoms occupy two distinct sites, 16a and 24d, of octahedral and tetrahedral symmetries, respectively. The Y atoms reside at the 24c sites of dodecahedral symmetry, whereas the O atoms occupy the general 96h positions [30].

The first-principles calculations in the present study were based on density-functional theory (DFT) and were performed with the aid of the ab-initio VASP code [31–34]. The valence wavefunctions were represented by an expansion of plane waves with the basis limited by a cutoff of 400 eV. The valence shells for the different elements are listed inside the brackets: Y[$4s^2$, $4p^6$, $4d^1$, $5s^2$], Al[$3s^2$, $3p^1$], O[$2s^2$, $2p^4$] and H[$1s^1$]. Core-valence interactions were described by pseudopotentials, constructed according to the projector-augmented wave (PAW) approach [35]. The semilocal PBE functional [23] was employed to describe exchange and correlation effects. Additionally, the HSE06 hybrid functional [25] was also used with a portion of exact nonlocal exchange, equal to 25%, admixed to the semilocal exchange. A band gap, E_{gap}, of 6.31 eV was obtained, in excellent agreement with experiment.

For the defect calculations the conventional 160-atom cubic cell was used fixing the lattice parameter to the experimental one, equal to 12 Å [29]. The corresponding integrations over the Brillouin zone were performed using a body-centered **k**-point mesh with two points, (0,0,0) and $(\frac{1}{2},\frac{1}{2},\frac{1}{2})$, in the irreducible part.

The formation energies of all vacancy and hydrogen defects were determined using the HSE06 functional. These energies are the excess energies [36] of the defects and depend upon the Fermi level, E_F, and the elemental chemical potentials, μ, according to:

$$\Delta E^{def}_{\rm form}(q) = E^{def}_{\rm tot}(q) - E^{bulk}_{\rm tot} + \textstyle\sum_{\rm i}(\Delta n_{\rm i})\mu_{\rm i} + qE_{\rm F} \tag{1}$$

where $E^{def}_{\rm tot}(q)$ and $E^{bulk}_{\rm tot}$ represent the total energies of the defect and bulk-crystalline supercells, respectively. q stands for the charge state of the defect. The quantity Δn enters with a value of $+1$ for a vacancy and -1 for a single interstitial hydrogen atom. The reference energy for the Fermi level is taken to be the valence-band top, E_V. The formation energies of charged defects (nonzero q) were corrected by adding an electrostatic term [37]. This correction accounts for the fictitious interactions of the charged defects with their periodic images.

The thermodynamic charge-transition levels, $\epsilon(q/q')$, are then defined as the Fermi-level positions in the gap where the defect states, q and q', possess the same formation energies.

The VESTA code [38] was used to display all minimum-energy atomistic structures of the defects after structural relaxation.

The calculations of the positron lifetimes of the vacancy defects were performed within two-component density-functional theory (TCDFT) [26–28] using the ABINIT code [39]. The corresponding implementation is based on the PAW formalism where the positron and electron densities, $n_+(\mathbf{r})$ and $n_-(\mathbf{r})$, respectively, within the supercells are represented with the same basis sets [40].

The total energy functional for the system of interpenetrating electron and positron densities under the influence of an external potential $V_{\rm ext}$ is given as follows [28]:

$$\begin{aligned} E[n_-, n_+] = {} & F[n_-] + F[n_+] \\ & + \int d\mathbf{r}\; V_{\rm ext}(\mathbf{r})[n_-(\mathbf{r}) - n_+(\mathbf{r})] \\ & - \iint d\mathbf{r}d\mathbf{r}' \frac{n_-(\mathbf{r})n_+(\mathbf{r})}{|\mathbf{r}-\mathbf{r}'|} \\ & + E_c^{e-p}[n_-, n_+] \end{aligned} \tag{2}$$

where F[n] is the conventional DFT single-component functional for either density. The quantity $E_c^{e-p}[n_-, n_+]$ represents the electron-positron correlation energy [28]. The latter was calculated by means of the generalized-gradient approximation for the electron-positron interaction. This approximation includes gradient corrections (GC), thus accounting for the effects of non-

uniform densities [41,42]. These corrections sample the local variations of the density, $n/\nabla|n|$, and depend upon the Thomas-Fermi screening length $1/q_{TF}$ [41]. The lowest-order term for GC, $\epsilon = |\nabla n|^2/(nq_{TF})^2$, provides the reduction of the screening strength at the positron site [41].

The Kohn-Sham equations are solved simultaneously for both $n_+(\mathbf{r})$ and $n_-(\mathbf{r})$ densities, by updating the positron density after the end of every electron iteration cycle [40]. The forces on the ions induced by the presence of the positron were also included in the energy minimization. The converged positron and electron densities were finally used to calculate the positron lifetime, τ, according to [28]:

$$\frac{1}{\tau} = \pi c r_o^2 \int d\mathbf{r}\ n_+(\mathbf{r})\ n_-(\mathbf{r})\ g(n_+, n_-) \qquad (3)$$

where c is the speed of light and r_o the classical radius of the electron. The intergrand depends upon the overlap between the electron and positron densities weighted by the enhancement factor, $g(n_+,n_-)$. The latter accounts for the induced polarization of the electron density due to the presence of the positron.

In the present study the functional forms for $g(n_+,n_-)$ were based on the LDA parametrization of Puska, Seitsonen and Nieminen evaluated in the random-phase approximation limit [43], with added gradient corrections [28,41]. The resulting enhancement factor, g_{GC}, is obtained as follows [41]:

$$g_{GC} = 1 + (g_{LDA} - 1)\ \exp(-\alpha\epsilon) \qquad (4)$$

where the parameter α has a value of 0.22. This magnitude was found to lead to very good agreement of the calculated GC-based positron lifetimes with experimental data for a number of materials [41,44].

The TCDFT calculations for the vacancy defects were performed using the same 160-atom cubic supercells. A plane-wave cutoff of 490 eV was chosen and the use of the Γ point of the supercell Brillouin zone was sufficient for the convergence of the positron lifetimes. Tests with four $\mathbf{k}$ points led to deviations of less than 1 ps. For the electron–electron exchange and correlation effects the PBE semilocal functional was employed.

3 Results

3.1 Defect-formation energies and charge-transition levels

The hydrogen impurity was placed at various interstitial positions inside the YAG lattice. Energy minimization was then performed that eventually lead to the lowest-energy equilibrium sites for hydrogen and for each possible charge state. The final formation energies following the structural relaxation are displayed in Fig. 1 for hydrogen-rich conditions. For these conditions the chemical potential of hydrogen is taken as half the total energy of an isolated hydrogen molecule, at T = 0 K. It can be inferred from the formation-energy results that hydrogen is an amphoteric defect in YAG with the pinning level, $\epsilon(+1/-1)$, inside the band gap. The neutral charge state is never thermodynamically stable for any Fermi-level position within the gap. Instead, in the largest part of the gap, hydrogen assumes a positively charged state, H^+, releasing its electron to the conduction band of the host. The atomistic structure of the positively charged hydrogen configuration is displayed in Fig. 2(a). It can be seen that the hydrogen nucleus resides in a bridge position between two oxygen atoms. This -O_{NN}–H–O_{NNN}- configuration is strongly asymmetrical and entails the formation of a short O-H bond with a bondlength, O_{NN}-H, equal to 1.02 Å, whereas the next nearest oxygen, O_{NNN}, is located at 1.52 Å from hydrogen. As it can be seen from Fig. 3(a) the positively-charged interstitial hydrogen does not introduce any defect levels inside the fundamental band gap of YAG. Instead, H^+ induces an O-H bonding state inside the valence band. This state is filled (doubly occupied) and it is seen to be split off the upper valence band of YAG by 0.47 eV. Its location is at 7.12 eV with respect to the valence-band edge.

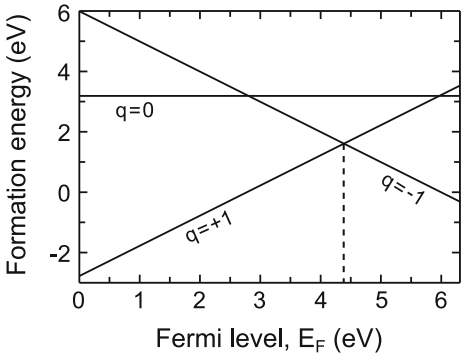

Fig. 1 Formation energies and charge states of hydrogen as a function of Fermi-level position in the theoretical (HSE06) band gap for hydrogen-rich conditions. The dashed vertical line denotes the thermodynamic $\epsilon(+1/-1)$ charge-transition level. The reference energy for the Fermi level is the valence-band top, E_V

Alternatively, hydrogen is predicted to be negatively charged in the upper part of the band gap, with the $\epsilon(+1/-1)$ transition level at: $E_C-1.92$ eV, where E_C is the conduction-band edge. In this case hydrogen resides at the empty 16*g* interstitial site; in this site the impurity is three-fold coordinated by the nearest yttrium ions. The corresponding Y-H distances are equal to 1.92 Å (see Fig. 2b). The effect of H^- to the YAG electronic structure is to introduce a filled (doubly occupied) state deep inside the band gap, see Fig. 3b. This state lies at 1.65 eV above the valence-band edge.

The situation for the Al monovacancies presents a complication since the aluminum ions of the cation sublattice occupy two distint crystallographic sites; the 16*a* site of octahedral oxygen coordination and the 24*d* one of tetrahedral coordination. Thus, two inequivalent

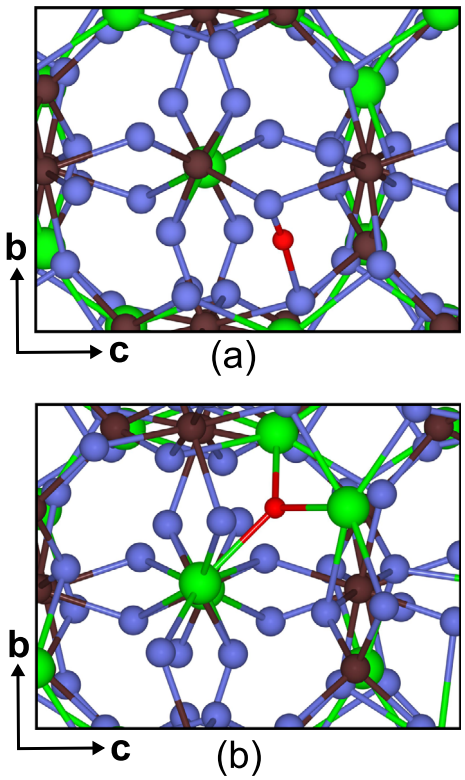

Fig. 2 Atomistic structures of the thermodynamically stable hydrogen configurations in YAG. **a** H^+ charge state. **b** H^- charge state. The different elements in the present figure and the ones that follow are represented as: oxygen by medium-sized blue spheres, yttrium by large green spheres, aluminum by small dark-brown spheres and hydrogen by the small red sphere

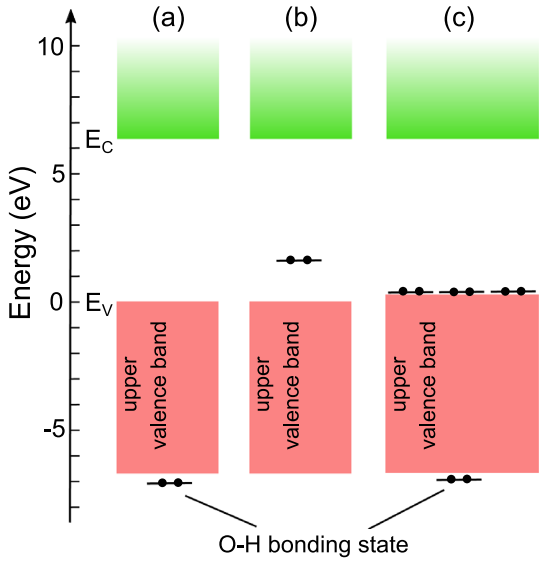

Fig. 3 Graphical depiction of the electron levels of hydrogen and vacancy defects in YAG, showing the defect-induced levels and their occupation. The plotted results correspond to the HSE06 single-particle energy eigenvalues obtained at the Γ point of the supercells. **a** Interstitial hydrogen, H^+ state. **b** Interstitial hydrogen, H^- state. **c** $(V_{Al_{oct}} - H)^{-2}$ defect. The reference energy is defined by the valence-band edge, E_V. E_C is the conduction-band minimum

monovacancy defects, $V_{Al_{oct}}$ and $V_{Al_{tet}}$, were created by removing the aluminum ions from these positions. The formation energies of these monovacancies were then determined for every possible charge state of these defects. The final formation-energy results are diplayed in Fig. 4. It can be seen that the $V_{Al_{tet}}$ vacancy has a lower energy with respect to $V_{Al_{oct}}$, irrespective of the Fermi-level position or charge state. Also, in agreement with previous DFT calculations [19,20], the present results show that both aluminum monovacancies are acceptor-like defects, and are negatively charged for most Fermi-level positions inside the gap. The q=−3 charge state is the dominant state in the band gap. The $\epsilon(-2/-3)$ charge-transition level lies deep inside the gap; at E_V+1.62 eV for the $V_{Al_{oct}}$ vacancy and at E_V+2.17 eV for the $V_{Al_{tet}}$ vacancy. It is also noteworthy that the neutral state for both vacancies is stable for a rather extended region of Fermi-level positions above the valence edge, E_V. The upper bound of this region is the $\epsilon(0/-1)$ transition level, which lies at 1.28 eV and 1.93 eV above E_V, for the $V_{Al_{oct}}$ and $V_{Al_{tet}}$ vacancies, respectively. This finding agrees very well with recent calculations [20] that employed the meta-GGA SCAN functional [45]; In contrast, calculations based on the semilocal GGA functional predicted an extremely small range of stability for the neutral charge state for both aluminum monovacancies [19], confined very near the valence-band edge, E_V.

The structures of both fully charged Al monovacancies (q=−3 state) are depicted in Fig. 5. The principal relaxation pattern for both vacancies is a uniform outward displacement of the nearest-neighbor oxygen ions, O_{NN}, away from the vacancy sites.

For the $V_{Al_{oct}}$ vacancy the distances of the six oxygen neighbors from the vacancy site are equal to 2.23 Å. This amounts to a 14.6% increase with respect to 1.92 Å, the Al_{oct}–O_{NN} distances in the perfect YAG lattice. For the $V_{Al_{tet}}$ vacancy the four O_{NN} neighbors reside at 2.04 Å away from the vacancy center. This displacement amounts to an increase of 13.6% of the Al_{tet}–O_{NN} distance of 1.77 Å, in the perfect YAG lattice. Thus, the $V_{Al_{oct}}$ vacancy is the defect with the larger free volume.

Association of hydrogen with the aluminum monovacancies was studied by energy minimization after placing a single hydrogen atom at various positions near the vacancies, considering a range of possible charge states from $q = -3$ to $q = +1$. In the ensuing structural relaxation hydrogen was found to bind to an oxygen atom that belongs to the nearest-neighbor shell of the vacancy. The formation energies of all stable charge states of the vacancy-hydrogen defect complexes are shown in Fig. 6.

The dominant charge state of the vacancy-hydrogen defects inside the gap is the q=−2 state, thus, these defects remain negatively charged for the largest part of the gap, up to the conduction-band edge. The ϵ(–

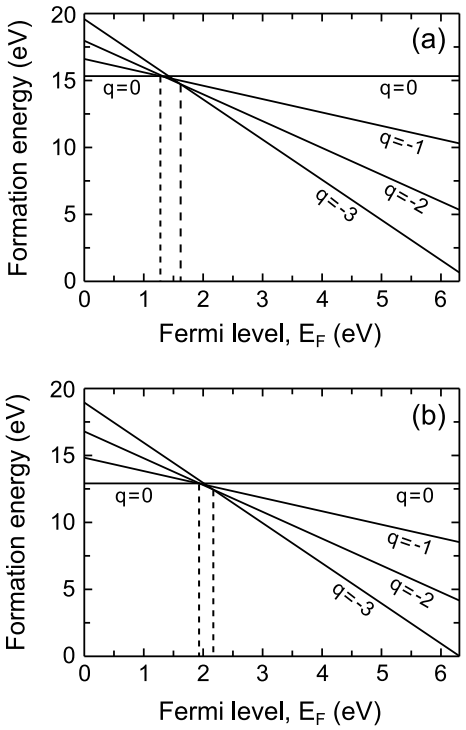

Fig. 4 Formation energies and charge states of Al monovacancies as a function of Fermi-level position in the theoretical (HSE06) band gap. **a** $V_{\mathrm{Al_{oct}}}$ vacancy. **b** $V_{\mathrm{Al_{tet}}}$ vacancy. The dashed vertical lines denote the $\epsilon(0/-1)$ and $\epsilon(-2/-3)$ charge-transition levels. The results were obtained with the HSE06 functional and correspond to aluminum-rich conditions. The reference energy for the Fermi level is the valence-band top, E_{V}

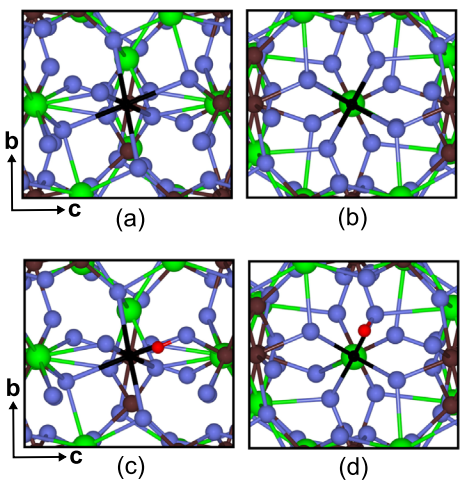

Fig. 5 Atomistic structures of aluminum monovacancies and vacancy-hydrogen defect complexes in YAG. The vacancy sites are depicted by the black spheres. **a** Fully charged octahedrally-coordinated Al monovacancy, $V^{-3}_{\mathrm{Al_{oct}}}$. **b** Fully charged tetrahedrally-coordinated Al monovacancy, $V^{-3}_{\mathrm{Al_{tet}}}$. **c** $(V_{\mathrm{Al_{oct}}} - \mathrm{H})^{-2}$ defect. **d** $(V_{\mathrm{Al_{tet}}} - \mathrm{H})^{-2}$ defect

1/–2) acceptor level lies at 1.58 eV and 1.97 eV above E_{V} for the $(V_{\mathrm{Al_{oct}}} - \mathrm{H})$ and $(V_{\mathrm{Al_{tet}}} - \mathrm{H})$ defects, respectively (see Fig. 6). The dominance of this charge state

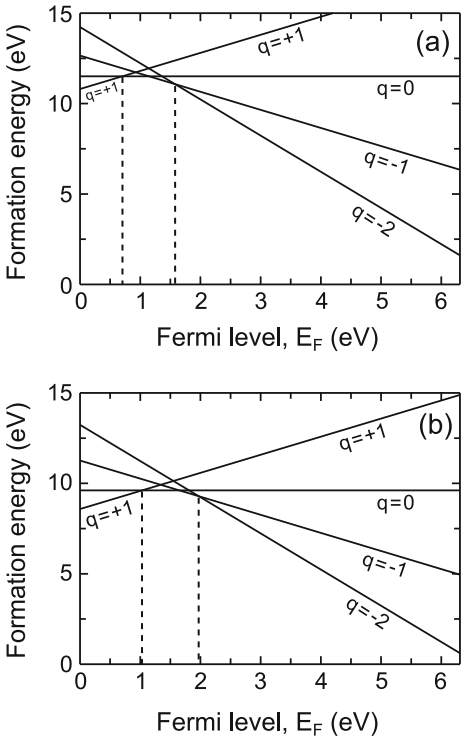

Fig. 6 Formation energies and charge states of the vacancy-hydrogen defect complexes as a function of the Fermi level in the theoretical (HSE06) band gap, for aluminum-rich conditions. (**a**) $(V_{\mathrm{Al_{oct}}} - \mathrm{H})^{q}$ defect. (**b**) $(V_{\mathrm{Al_{tet}}} - \mathrm{H})^{q}$ defect. The dashed vertical lines denote the $\epsilon(+1/0)$ and $\epsilon(-1/-2)$ charge-transition levels. The energy reference for the Fermi-level positions is the valence-band top, E_{V}

suggests that the nominally fully charged aluminum monovacancies (q=−3) associate most favourably with hydrogen when the latter carries a positive charge of q=+1, namely, H^{+}. This association leads to a vacancy-hydrogen defect in a q=−2 charge state, namely: $(V_{\mathrm{Al}} - \mathrm{H})^{-2}$. The atomistic structures of these defects are shown in Fig. 5c, d. In these defects the corresponding O-H bondlength is 0.99 Å for both types of aluminum monovacancies; this magnitude is shorter than the O-H distance found for the isolated H^{+} configuration and indicates a stronger covalent interaction with the oxygen atom. A comparison also with the local environment of the aluminum monovacancies also shows that hydrogen induces a local compression to the lattice near the vacancy sites: for the $(V_{\mathrm{Al_{oct}}} - \mathrm{H})^{-2}$ defect the six $\mathrm{O_{NN}}$ atoms are now found found at distances of 2.20 Å and less from the vacancy center, with the oxygen atom bonded to hydrogen displacing towards the vacancy and residing at 1.97 Å from it. A similar compression is also observed for the $(V_{\mathrm{Al_{tet}}} - \mathrm{H})^{-2}$ defect, with the vacancy-oxygen distances less than 2.02 Å, and the nearest oxygen atom bonded to hydrogen found at 1.81 Å away from the vacancy center. Thus, the presence of hydrogen near both Al monovacancies reduces the free volume of either of these

defects. Inspection of the electronic structures of the $(V_{\mathrm{Al}}-\mathrm{H})^{-2}$ defects shows no defect-induced levels deep inside the fundamental band gap of YAG; see Fig. 3(c). Again, the O-H bonding state appears just below the upper valence band, whereas the vacancy levels appear as a triplet of filled electron levels extremely near the valence-band edge (to within 0.20 eV from $\mathrm{E_V}$). The upper valence states for this defect were also found to protrude slightly inside the band gap, thus, raising the valence-band maximum with respect to the defect-free bulk crystal. Figure 3(c) depicts the electron levels for the $(V_{\mathrm{Al_{oct}}}-\mathrm{H})^{-2}$ defect. The corresponding levels for the $(V_{\mathrm{Al_{tet}}}-\mathrm{H})^{-2}$ defect are qualitatively very similar.

It is also instructive to examine the energetic stability of the $(V_{\mathrm{Al}}-\mathrm{H})^{-2}$ defect complex, in particular, how easy it is to dissociate into the V_{Al}^{-3} and H^{+} single defects. These defects carry opposite charges and should be expected to mutually attract each other through their electrostatic coupling. However, other terms originating from exchange, overlap and Hartree interactions will also contribute. A quantitative measure of the total interaction is the binding energy, $\mathrm{E_b}$. This quantity can be obtained from the energy balance of the respective formation energies. Namely:

$$E_{\mathrm{b}} = \Delta E_{\mathrm{form}}[(V_{\mathrm{Al}}-\mathrm{H})^{-2}] - \Delta E_{\mathrm{form}}[V_{\mathrm{Al}}^{-3}] - \Delta E_{\mathrm{form}}[\mathrm{H}^{+}] \quad (5)$$

A negative sign for $\mathrm{E_b}$ would mean that the defect complex is stable against dissociation. The calculated binding energies for the lowest-energy $(V_{\mathrm{Al}}-\mathrm{H})^{-2}$ configurations, for either vacancy, were found equal to −1.65 eV, and −2.02 eV, for the vacancy defects involving the $V_{\mathrm{Al_{oct}}}$ and $V_{\mathrm{Al_{tet}}}$ vacancies, respectively. Therefore, both defect complexes are stable with respect to an isolated interstitial H^{+} and a bare Al vacancy, V_{Al}^{-3}. From the calculated numerical values of $\mathrm{E_b}$ it can also be concluded that hydrogen is more strongly bound to the lower-energy $V_{\mathrm{Al_{tet}}}$ vacancy.

Further inspection of the formation-energy plot of Fig. 6 shows that the vacancy-hydrogen complexes are positively charged defects for Fermi-level positions near the valence band. These regions are dictated by the $\epsilon(+1/0)$ transition level; this level lies at E_{V}+0.71 eV and E_{V}+1.03 eV, for the two different vacancy-hydrogen defects.

3.2 Positron trapping and lifetimes of the vacancy-hydrogen defects

It was proposed in earlier PALS studies [10,11] that the aluminum vacancies are dominant positron-trapping centers in YAG single crystals. The reported positron lifetimes for several YAG samples prepared under various conditions were found to be considerably longer with respect to the bulk lifetimes [10]. This was corroborated by first-principles calculations based on TCDFT where indeed it was found that aluminum monovacancies and their defect complexes can give rise to positron lifetimes in excess of 200 ps [19]. In contrast, oxygen monovacancies are positively charged in the largest part of the YAG gap [16,19,20]; thus, they are not expected to trap positrons. Also, TCDFT calculations of the positron lifetimes of neutral oxygen monovacancies led to positron lifetimes for these defects considerably smaller to those obtained for the cation monovacancies [19]. Other defects in YAG, such as cation antisites and interstitial defects, even if negatively charged, can only act as shallow traps for positrons. In such shallow positron traps the positronic wavefunctions form spatially extended hydrogenic states (with a typical range of 10–100 Å) that probe mainly the defect-free perfect lattice [13].

However, when the YAG samples were grown under a hydrogen-rich atmosphere the measured positron lifetimes were found to decrease considerably [10]. These observations are consistent with existing theoretical studies in metals [46], ZnO [47] and zirconia phases [48,49] where hydrogen decoration of vacancies was found to have a strong effect on positron annihilation leading to a reduction of the positron lifetimes.

To assess the impact of hydrogen to the character of positron states in YAG TCDFT calculations were performed for the lowest-energy $(V_{\mathrm{Al}}-\mathrm{H})^{-2}$ defect complexes, as well for the fully charged monovacancy defects (bare vacancies), $V_{\mathrm{Al_{oct}}}^{-3}$ and $V_{\mathrm{Al_{tet}}}^{-3}$, which are known to trap positrons. The real-space positron densities for the bare vacancies and these vacancy-hydrogen complexes are displayed in Fig. 7a, b, e, f. It can be seen that all of these defects are capable of positron trapping, since a sizeable portion of the positron density is confined within the available free space at and near the vacancy sites. The higher-value isodensity level (pink color) corresponds to 72% of the maximum density, whereas the more extended isodensity (in yellow) to 33% of the maximum density.

The calculated positron lifetimes for all vacancy-hydrogen defects are displayed in Fig. 8. In the same Figure the range of bulk lifetimes reported for YAG single crystals is also depicted together with the theoretical bulk lifetime. The latter is equal to 161 ps. The measured bulk lifetimes are within a range from 147 ps to 166 ps for YAG samples, depending upon treatment, composition and growth conditions [10]. Clearly, hydrogen has a strong impact: the presence of hydrogen in the vicinity of the bare aluminum vacancies leads to a reduction of the magnitude of the calculated lifetimes. Whereas, the magnitude of the positron lifetimes equals 234 ps and 230 ps for the bare monovacancies, $V_{\mathrm{Al_{oct}}}^{-3}$ and $V_{\mathrm{Al_{tet}}}^{-3}$, respectively, there is a net drop of lifetimes for the $(V_{\mathrm{Al}}-2\mathrm{H})^{-1}$ defects, with magnitudes of 208 ps and 205 ps, respectively.

Hydrogen decoration was more extensively addressed by the introduction of more hydrogen ions, H^{+}, near the vacancies. During structural relaxation these ions were eventually found to bind to the oxygen atoms that belong to the nearest-neighbor shell of each vacancy (see Fig. 7). The H^{+} ions provide a charge compensation mechanism which renders the vacancy-hydrogen defects progressively less negatively charged, and even-

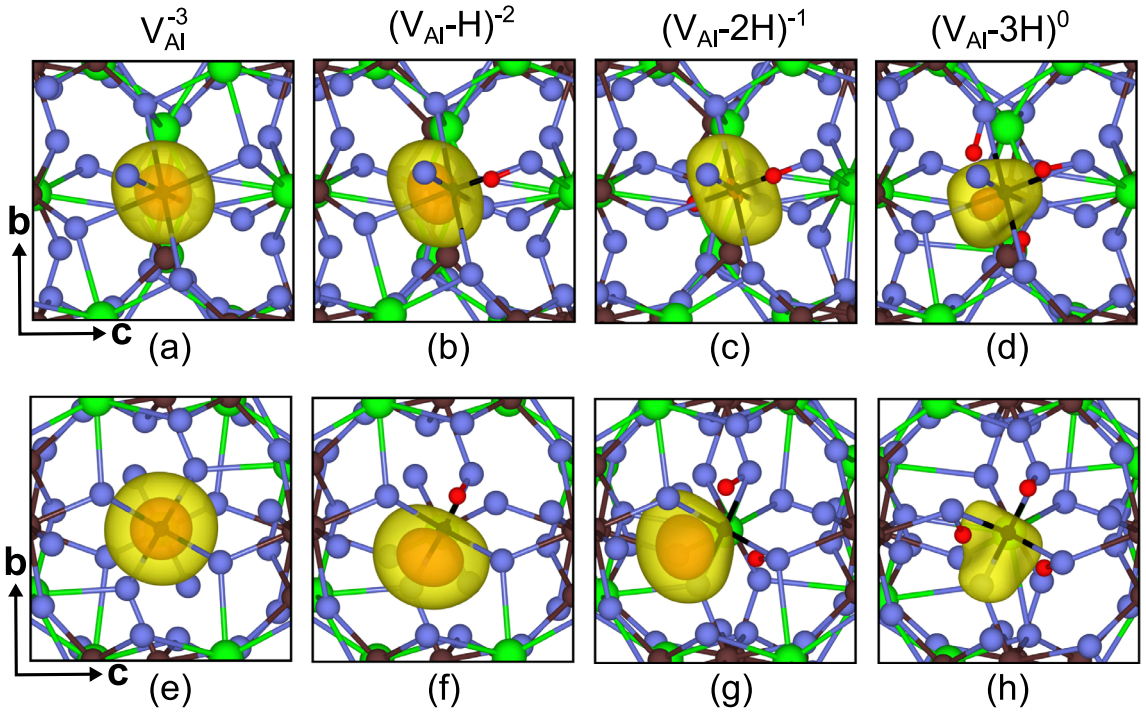

Fig. 7 Real-space positron densities of the bare vacancies and the vacancy-hydrogen defects, calculated by the TCDFT-GC scheme. The upper panel shows the defects that the $V_{\mathrm{Al_{oct}}}$ vacancy forms. The lower panel shows the defects of the $V_{\mathrm{Al_{tet}}}$ vacancy. Two isosurface densities of different intensities are displayed: the interior isosurface (pink color) corresponds to an isosurface level of 0.013 $e^+/Å^3$. The more extended one (yellow color) corresponds to an isosurface level of 0.006 $e^+/Å^3$

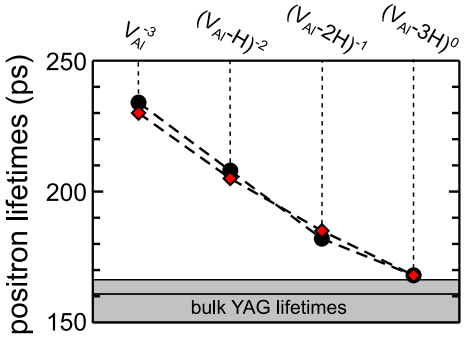

Fig. 8 Positron lifetimes (in ps) of vacancy-hydrogen defects in YAG, calculated by the TCDFT-GC scheme. Filled black circles (red diamonds) correspond to the defects formed by the $V_{\mathrm{Al_{oct}}}$ ($V_{\mathrm{Al_{tet}}}$) vacancies. The grey-shaded region from 150 to 166 ps corresponds to the range of bulk lifetimes measured for various YAG single crystals [10]. The theoretical bulk lifetime for the YAG solid, calculated using gradient corrections, is equal to 161 ps and is also indicated by the horizontal line

tually charge neutral for a defect complex consisting of a single aluminum monovacancy decorated by three H^+ ions. Thus, two additional vacancy-hydrogen complexes were formed, namely, $(V_{\mathrm{Al}} - 2\mathrm{H})^{-1}$ and $(V_{\mathrm{Al}} - 3\mathrm{H})^0$.

The real-space positron densities of all these defects can be seen in Fig. 7. Again, localization of the positron densities is observed at and near the vacancy sites for all vacancy-hydrogen defects, albeit with certain qualitative differences. The degree of localization is substantially stronger for the bare V_{Al}^{-3} monovacancies and the $(V_{\mathrm{Al}} - \mathrm{H})^{-2}$ defects. For these cases positron densities of larger intensity are obtained at and near the defect sites. It can also be seen that the hydrogen nuclei bound near the vacancies cause a shift of the positron densities away from the vacancy sites (see Fig. 7). Thus, for a number of vacancy-hydrogen complexes the positron-density maxima no longer coincide with the geometrical location of the vacancy sites. In contrast, in the bare monovacancies the maxima of the positron densities are centered at the vacancy sites.

The presence of two or more hydrogen ions near the vacancies decreases the positron lifetimes to less than 200 ps (see Fig. 8). For the neutral vacancy-hydrogen defects, $(V_{\mathrm{Al}} - 3\mathrm{H})^0$, a lifetime of 168 ps is obtained. This value is marginally longer to the reported bulk-crystal YAG lifetimes and to the calculated bulk lifetime of YAG (161 ps).

The impact of hydrogen to the decrease of the positron lifetimes very likely originates from two effects: (a) the presence of hydrogen ions, H^+, near the vacancies leads to a decrease of the intensities of the positron densities within the free space of the vacancies. This probably is caused by the less negative (even neutral) charge states of the vacancy-hydrogen defects that give rise to more shallow potential wells for the positrons. The positron densities become, thus, more delocalized. (b) Owing to their positive charge, the H^+ ions repel and eventually displace the positron densities (see

Fig. 7). As a consequence of both of these effects the overlap of positron and electron densities increases, thus, on account of Eq. 3 the magnitude of the corresponding lifetimes will be smaller.

Overall, the present results appear to justify earlier interpretations on the impact of hydrogen on positron trapping in YAG. However, this agreement is not strictly quantitative since full passivation is not attained; all vacancy-hydrogen complexes that were studied exhibit some residual positron localization with corresponding lifetimes slightly longer to the bulk YAG lifetimes.

4 Conclusions

First-principles calculations based on the hybrid HSE06 functional were performed to study the hydrogen impurity in YAG and its interaction and binding with the aluminum monovacancies. The calculations provided the microscopic structures of these defects, the defect-induced electron levels and their stable charge states as a function of the Fermi-level position in the gap. Hydrogen is predicted to be an amphoteric defect in YAG, being positively charged in the largest part of the band gap. Single hydrogen atoms were found to associate favourably with both the octahedrally- and the tetrahedrally-coordinated fully-charged aluminum monovacancies forming stable vacancy-hydrogen complexes with negative binding energies. These defect complexes do not introduce any deep trap levels within the YAG gap; instead, they give rise to shallow, filled levels just above the valence-band edge. Structurally, this binding leads to a local compression of the lattice, decreasing the free volume of the vacancy defects.

The effects of hydrogen on positron trapping in YAG were further explored by means of two-component DFT calculations. The character of positron trapping and associated lifetimes were obtained for a number of vacancy-hydrogen defect complexes as a function of the number of hydrogen atoms bound to the vacancies. Hydrogen decoration modified the positron densities near the vacancies and led to a sizeable decrease of the positron lifetimes. Taking also into consideration that the vacancy-hydrogen complexes are predicted to be positively charged for Fermi-level positions near the valence-band edge (and thus would repel positrons), the present results suggest that the presence of hydrogen in YAG should partially impair the ability of aluminum monovacancies to trap positrons.

Acknowledgements. This work was financially supported by FEDER (Programa Operacional Factores de Competitividade COMPETE) and FCT Portugal - Fundação para a Ciência e Tecnologia under the UID/FIS/04564/2016 and PTDC/FIS-MAC/29696/2017 projects. The computer resources of the Department of Physics of the University of Coimbra were used, including the Navigator cluster at the Laboratory for Advanced Computing.

Data availability The datasets generated during and/or analysed during the current study are available from the corresponding author on reasonable request. This manuscript has no associated data or the data will not be deposited. [Author's comment: More detailed data of the present study can be provided from the author on reasonable request.]

References

1. R.C. Powell, *in Physics of Solid State Laser Materials* (Springer, New York, 1998)
2. J. Ueda, S. Tanabe, Opt. Mater.: X **1**, 100018 (2019)
3. D.J. Robbins, B. Cockayne, B. Lent, C.N. Duckworth, J.L. Glasper, Phys. Rev. B **19**, 1254 (1979)
4. C.R. Varney, D.T. Mackay, A. Pratt, S.M. Reda, F.A. Selim, J. Appl. Phys. **111**, 063505 (2012)
5. D.T. Mackay, C.R. Varney, J. Buscher, F.A. Selim, J. Appl. Phys. **112**, 023522 (2012)
6. P. Dorenbos, J. Lumin. **134**, 310 (2013)
7. E. Zych, C. Brecher, J. Glodo, J. Phys.: Condens. Matter **12**, 1947 (2000)
8. D. Winarski, C. Persson, F.A. Selim, Appl. Phys. Lett. **105**, 221110 (2014)
9. C.R. Varney, D.T. Mackay, S.M. Reda, F.A. Selim, J. Phys. D Appl. Phys. **45**, 015103 (2012)
10. F.A. Selim, C.R. Varney, M.C. Tarun, M.C. Rowe, G.S. Collins, M.D. McCluskey, Phys. Rev. B **88**, 174102 (2013)
11. F.A. Selim, D. Winarski, C.R. Varney, M.C. Tarun, J. Ji, M.D. McCluskey, Results Phys. **5**, 28 (2015)
12. M.J. Puska, R.M. Nieminen, Rev. Mod. Phys. **66**, 841 (1994)
13. F. Tuomisto, I. Makkonen, Rev. Mod. Phys. **85**, 1583 (2013)
14. L. Schuh, R. Metselaar, C.R.A. Catlow, J. Eur. Ceram. Soc. **7**, 67 (1991)
15. M.M. Kuklja, R. Pandey, J. Am. Ceram. Soc. **82**, 2881 (1999)
16. J. Chen, T.C. Lu, Y. Xu, A.G. Xu, D.Q. Chen, J. Phys.: Condens. Matter **20**, 325212 (2008)
17. B. Liu, M. Gu, X. Liu, S. Huang, C. Ni, Appl. Phys. Lett. **94**, 121910 (2009)
18. Z. Li, B. Liu, J. Wang, L. Sun, J. Wang, Y. Zhou, J. Am. Ceram. Soc. **95**, 3628 (2012)
19. A.G. Marinopoulos, Eur. Phys. J. B **92**, 242 (2019)
20. W. Lafargue-Dit-Hauret, M. Allix, B. Viana, S. Jobic, C. Latouche, Theor. Chem. Acc. **141**, 58 (2022)
21. Y.-N. Xu, W.Y. Ching, Phys. Rev. B **59**, 10530 (1999)
22. A.B. Munoz-Garcia, E. Anglada, L. Seijo, Intl. J. Quantum Chemistry **109**, 1991 (2009)
23. J.P. Perdew, K. Burke, M. Ernzerhof, Phys. Rev. Lett. **77**, 3865 (1996)
24. G.A. Slack, D.W. Oliver, R.M. Chrenko, S. Roberts, Phys. Rev. **177**, 1308 (1969)
25. M. Marsman, J. Paier, A. Stroppa, G. Kresse, J. Phys.: Condens. Matter **20**, 064201 (2008)
26. B. Chakraborty, Phys. Rev. B **24**, 7423 (1981)
27. B. Chakraborty, R.W. Siegel, Phys. Rev. B **27**, 4535 (1983)
28. E. Borónski, R.M. Nieminen, Phys. Rev. B **34**, 3820 (1986)

29. F. Euler, J.A. Bruce, Acta Crystallogr. **19**, 971 (1965)
30. S. Geller, Z. Kristallogr. **125**, 1 (1967)
31. G. Kresse, J. Hafner, Phys. Rev. B **47**, 558 (1993)
32. G. Kresse, J. Hafner, Phys. Rev. B **49**, 14251 (1994)
33. G. Kresse, J. Furthmüller, Phys. Rev. B **54**, 11169 (1996)
34. G. Kresse, D. Joubert, Phys. Rev. B **59**, 1758 (1999)
35. P.E. Blöchl, Phys. Rev. B **50**, 17953 (1994)
36. S.B. Zhang, J.E. Northrup, Phys. Rev. Lett. **67**, 2339 (1991)
37. G. Makov, M.C. Payne, Phys. Rev. B **51**, 4014 (1995)
38. K. Momma, F. Izumi, J. Appl. Crystallogr. **44**, 1272 (2011)
39. X. Gonze, F. Jollet, F. Abreu Araujo, D. Adams, B. Amadon, T. Applencourt, C. Audouze, J.-M. Beuken, J. Bieder, A. Bokhanchuk, E. Bousquet, F. Bruneval, D. Caliste, M. Côté, F. Dahm, F. Da Pieve, M. Delaveau, M. Di Gennaro, B. Dorado, C. Espejo, G. Geneste, L. Genovese, A. Gerossier, M. Giantomassi, Y. Gillet, D.R. Hamann, L. He, G. Jomard, J. Laflamme Janssen, S. Le Roux, A. Levitt, A. Lherbier, F. Liu, I. Lukačević, A. Martin, C. Martins, M.J.T. Oliveira, S. Poncé, Y. Pouillon, T. Rangel, G.-M. Rignanese, A.H. Romero, B. Rousseau, O. Rubel, A.A. Shukri, M. Stankovski, M. Torrent, M.J. Van Setten, B. Van Troeye, M.J. Verstraete, D. Waroquiers, J. Wiktor, B. Xu, A. Zhou, J.W. Zwanziger, Comput. Phys. Commun. **205**, 106 (2016)
40. J. Wiktor, G. Jomard, M. Torrent, Phys. Rev. B **92**, 125113 (2015)
41. B. Barbiellini, M.J. Puska, T. Torsti, R.M. Nieminen, Phys. Rev. B **51**, 7341 (1995)
42. B. Barbiellini, M.J. Puska, T. Korhonen, A. Harju, T. Torsti, R.M. Nieminen, Phys. Rev. B **53**, 16201 (1996)
43. M.J. Puska, A.P. Seitsonen, R.M. Nieminen, Phys. Rev. B **52**, 10947 (1995)
44. J. Kuriplach, B. Barbiellini, Phys. Rev. B **89**, 155111 (2014)
45. J. Sun, A. Ruzsinszky, J.P. Perdew, Phys. Rev. Lett. **115**, 036402 (2015)
46. H.E. Hansen, R.M. Nieminen, M.J. Puska, J. Phys. F: Met. Phys. **14**, 1299 (1984)
47. G. Brauer, W. Anwand, D. Grambole, J. Grenzer, W. Skorupa, J. Cížek, J. Kuriplach, I. Procházka, C.C. Ling, C.K. So, D. Schulz, D. Klimm, Phys. Rev. B **79**, 115212 (2009)
48. O. Melikhova, J. Kuriplach, J. Čížek, I. Procházka, G. Brauer, W. Anwand, J. Phys: Conf. Ser. **225**, 012035 (2010)
49. A.G. Marinopoulos, J. Phys.: Condens. Matter **31**, 315503 (2019)